Posterior parietal cortex regulates neural timescales and stimulus-driven attentional modulation in the prefrontal cortex

Orhan Soyuhos[1,2], Tirin Moore[5], Rishidev Chaudhuri[1,3,4], and Xiaomo Chen[1,3,6,*]

[1]Center for Neuroscience, University of California, Davis, Davis, CA, USA
[2]Department of Psychology, University of California, Davis, Davis, CA, USA
[3]Department of Neurobiology, Physiology and Behavior, University of California, Davis, Davis, CA, USA
[4]Department of Mathematics, University of California, Davis, Davis, CA, USA
[5]Department of Neurobiology, Howard Hughes Medical Institute, Stanford University, Stanford, CA, USA
[6]Lead contact
[*]Correspondence: xmch@ucdavis.edu

Abstract

Intrinsic neural timescales characterize the dynamics of endogenous fluctuations in neural activity. We measured the intrinsic timescales of prefrontal neurons and examined their changes during posterior parietal cortex (PPC) inactivation. Frontal eye field (FEF) neurons within the prefrontal cortex (PFC) exhibited a bimodal distribution of timescales: short-timescale neurons showed stronger transient visual responses, while long-timescale neurons exhibited stronger sustained modulation during stimulus-driven attention. PPC inactivation increased intrinsic timescales in both neuron types, with a 15-fold greater increase in short-timescale neurons. Additionally, it reduced visual and attentional modulation, particularly impairing attentional modulation in long-timescale neurons. Our results provide the first causal evidence that the intrinsic timescales of FEF neurons depend on PPC and suggest the presence of at least two network motifs with distinct timescales that contribute to neuronal dynamics and functional computations within FEF. The heterogeneity in these timescales may facilitate cognitive flexibility, allowing PFC to adapt to varying task demands.

Main

Intrinsic neural timescales measure the duration over which spontaneous neural activity remains temporally correlated with its past states, independent of external stimuli or specific behavioral tasks (Cavanagh et al., 2020; Murray et al., 2014; Wolff et al., 2022). They define the temporal window in which past neural activity can influence current neuronal dynamics, thereby shaping the processing and integration of information within neural circuits (Hasson et al., 2015). These timescales vary significantly across different brain regions, reflecting each area's specialized functional roles. For instance, along the visual hierarchy, early visual areas exhibit shorter intrinsic timescales, whereas higher-order areas demonstrate longer timescales (Chaudhuri et al., 2015; Murray et al., 2014). This gradient aligns with functional hierarchies in the brain, where shorter timescales are associated with regions involved in rapid information processing, and longer timescales support sustained cognitive functions, such as working memory and decision-making (Cavanagh et al., 2016; Wasmuht et al., 2018). Furthermore, the variability of intrinsic timescales among neurons within a cortical area corresponds to the functional specialization of

individual neurons (Cavanagh et al., 2020; Zeraati et al., 2023). Thus, the diversity of intrinsic neural timescales both across and within brain regions is fundamental to understanding how the brain integrates and segregates information over time (Cavanagh et al., 2020; Golesorkhi et al., 2021; Hasson et al., 2015; Wolff et al., 2022).

In the primate brain, the frontal eye field (FEF) and the posterior parietal cortex (PPC) are key areas within the frontoparietal attention network, with the PPC located earlier and the FEF positioned later in the visual hierarchy (Boshra and Kastner, 2022). Both areas are involved in representing stimulus-driven and goal-directed visual attention (Moore and Zirnsak, 2017; Xia et al., 2024). More recently, our research demonstrated a causal role of the PPC in regulating stimulus-driven attentional representations in the FEF and influencing behavioral outcomes (Chen et al., 2020). Anatomically, the FEF and oculomotor areas within the PPC, such as the lateral intraparietal area (LIP), are heavily reciprocally connected (Lynch and Tian, 2006). This interaction between the FEF and PPC is believed to play a crucial role in various cognitive functions, including visual attention (Murray et al., 2017; Hart and Huk, 2020). Moreover, the FEF receives direct projections from most of the functionally defined areas within the visual cortex (Schall et al., 1995) and sends feedback projections to the majority of the visual cortex (Schall et al., 1995; Stanton et al., 1995). Therefore, the FEF is thought to act as a proxy for prefrontal cortex communication with visual areas through these anatomical connections (Anderson et al., 2011). In this context, FEF intrinsic timescales likely play an important role in shaping the modulatory effect of attention on visual processing by determining the influence of past neural states on ongoing activity (Wasmuht et al., 2018).

The variation in intrinsic neural timescales across cortical areas is believed to be closely associated with both inter- and intra-area connectivity (Wang, 2020). Studies on the mechanisms underlying these timescales have traditionally emphasized the role of local and regional factors within the brain, such as dendritic spine density in pyramidal neurons (Elston, 2000, 2003; Elston et al., 2011), the expression levels of NMDA and GABA receptor genes (Gao et al., 2020; Wang, 2008; Wong and Wang, 2006), and the extent of structural and functional connectivity (Hart and Huk, 2020; Fallon et al., 2020). More recently, computational studies have linked the variation in intrinsic timescales across cortical areas to both inter- and intra-area connectivity (Chaudhuri et al., 2014, 2015; Wang, 2020). These models show that neural connectivity underpins these timescales, demonstrating that a hierarchy of timescales can emerge naturally from biophysically detailed models (Chaudhuri et al., 2015; Demirtaş et al., 2019). Moreover, they suggest that intrinsic timescales arise from a combination of diverse excitatory and inhibitory connection strengths within regions and long-range connectivity patterns, indicating that neither factor alone is sufficient to predict a region's timescales (Chaudhuri et al., 2014, 2015; Litwin-Kumar and Doiron, 2012). However, despite this evidence, the direct causal link between intra-area connectivity and intrinsic neural timescales remains untested. For instance, it is entirely unknown whether the intrinsic timescales of FEF neurons depend on the input from PPC.

In this study, we first examined the diversity of intrinsic neural timescales among individual neurons in the FEF. Next, we explored how these intrinsic timescales measured during the baseline fixation period relate to the functional specialization of FEF neurons during visual processing and stimulus-driven attentional modulation. Finally, we investigated the dependence of intrinsic timescales and functional properties of FEF neurons on the input from the PPC. Our findings revealed that FEF neurons exhibited a bimodal distribution of intrinsic neural timescales, with distinct groups characterized by either fast or slow timescales. Moreover, these timescales measured during the task-free baseline period were linked to the neurons' functional properties during the task. Short-timescale (short τ) neurons were more involved in processing transient visual responses, while long-timescale (long τ) neurons were more involved in sustained stimulus-driven attentional modulation. Furthermore, PPC inactivation selectively increased the intrinsic timescales of short τ neurons while reducing the attentional modulation of long τ neurons. These

findings highlight the causal role of the PPC in regulating both intrinsic neuronal dynamics and stimulus-driven attentional modulation in FEF.

Results

We recorded spiking activity within the FEFs in two behaving monkeys (J and Q) using multi-channel microelectrodes (see Methods; Fig. 1A). Within each trial, we measured the spiking responses to different visual stimulus patterns, including a single visual probe (Single) or a unique stimulus (Popout) (Fig. 1B). Additionally, we reversibly inactivated the PPC of these two monkeys via cryoloops that were chronically implanted within the intraparietal sulcus (IPS) and compared the spiking activity within the FEF with parietal inactivation (Inactivation condition) and without parietal inactivation (Control condition). In total, the spiking activity of 400 single- and multi-units was recorded from 192 FEF sites over 11 recording sessions.

Two distinct neural timescales in FEF neurons

To assess the diversity of intrinsic neuronal dynamics among individual neurons in the FEF, we first analyzed neural timescales across two monkeys without PPC inactivation (control condition). Specifically, we calculated the autocorrelation values for each neuron using endogenous fluctuations in spiking activity during the baseline period before stimulus presentation (Fig. 1C). We then fitted a single exponential decay function to these autocorrelation values to determine the intrinsic neural timescale for each neuron (Fig. 1D) (Murray et al., 2014). A relatively long τ indicated that intrinsic neural activity was sustained over extended periods with a stable firing pattern, whereas a short τ signified more transient activity characterized by a dynamic baseline firing pattern. We used pseudo-R-squared values to quantify the goodness of fit between our model and the observed data (Fig. 1SA). Overall, the exponential function closely aligned with the autocorrelation profiles of each neuron (mean R-squared = 0.78; Monkey J = 0.73; Monkey Q = 0.83). We excluded 20 units with R-squared values smaller than 0.3, ending up with 380 neurons for the control condition.

The probability density of timescale values for FEF neurons exhibited a bimodal distribution (Fig. 2A), confirmed by several statistical tests (Table S1). This bimodality was observed across both monkeys (Excess Mass Test: $p = 2 \times 10^{-3}$) and within each monkey individually (Excess Mass Test: Monkey Q: $p < 2.2 \times 10^{-16}$; Monkey J: $p = 2 \times 10^{-2}$) (Ameijeiras-Alonso et al., 2019). We then divided the neurons into short τ and long τ groups using the global minimum of the kernel density estimate (60.95 ms), derived from the combined distribution across both monkeys. These global minima were consistent across individual monkeys (Monkey J = 60.51 ms; Monkey Q = 59.33 ms) (Fig. 2B). As a result, neurons in the short τ group exhibited a fast decay rate ($N = 168$, Mean = 27.34 ms), whereas neurons in the long τ group showed a slower decay rate in their autocorrelation values during the baseline period ($N = 212$, Mean = 102.64 ms) (Fig. 2C). Similar distributions were observed for both Monkey J and Q (short τ neurons: Monkey J = 28.17 ms; Monkey Q = 26.71 ms; long τ neurons: Monkey J = 104.78 ms; Monkey Q = 100.73 ms). In contrast, the distributions of firing rates followed a unimodal pattern in each monkey (Excess Mass Test: Monkey Q, $p = 0.53$; Monkey J, $p = 0.78$) (Fig. S6B). These results suggest the presence of at least two network motifs within FEF with fast and slow neuronal dynamics.

Functional relevance of FEF intrinsic neural timescales

Next, we asked whether the intrinsic neural timescales measured during the task-free baseline period correlate with the neurons' functional properties during the task. We used visual and popout indices to quantify neuronal visual response and attentional modulation. Specifically, the visual index was calculated by comparing the activity evoked by a single stimulus presented inside versus outside the receptive field (RF). This index captures the spatial selectivity of visual responses, reflecting the ability of neurons to distinguish stimuli within their RFs. Similarly, a popout index was calculated by comparing neuronal response to unique stimuli inside versus outside the RF. This index quantifies stimulus-driven attentional modulation, reflecting the ability of neurons to distinguish visually salient stimuli. To further characterize temporal dynamics of these responses, we further divided the neuronal activity into transient (50–200 ms) and sustained (200–500 ms) periods following stimulus onset. This temporal segmentation allowed us to calculate transient and sustained versions of both the visual and popout indices, enabling us to distinguish rapid, short-lived neural responses to stimulus onset from long-term changes in neural activity associated with sustained modulation (see Methods).

To quantify the functional relevance of FEF neurons' intrinsic timescales, we used multiple linear regression analysis to identify relationships between these timescales and both visual and popout indices during transient and sustained epochs. Here, multiple linear regression analysis allowed us to assess correlation between intrinsic neural timescales and each predictor, while controlling for the influence of other predictors. For visual responses, our results revealed a significant negative association between timescales and transient visual indices (Permutation test: $p = 2 \times 10^{-4}$, $\beta = -73.98$). That is, neurons with fast intrinsic timescales showed a stronger response to single visual stimuli within their receptive field than neurons with slower intrinsic timescales. In contrast, for attentional modulation, there was a significant negative relationship between timescales and transient popout indices (Permutation test: $p = 2.05 \times 10^{-2}$, $\beta = -53.98$), as well as a significant positive relationship with sustained popout indices (Permutation test: $p = 9 \times 10^{-4}$, $\beta = 77.18$). In other words, neurons with slower intrinsic timescales exhibited stronger sustained attentional modulation, while neurons with faster timescales showed greater transient attentional modulation (Fig. 3A). These findings demonstrate a robust correlation between individual FEF neurons' intrinsic timescales and both their visual response and attentional modulation.

Given the clear functional relevance of FEF intrinsic timescales, we next asked whether visual responses and attentional modulation differ between two distinct groups of FEF neurons, defined by their intrinsic timescales during task-free activity (Fig. 3B). To answer this question, we first compared the visual and popout indices between short and long τ neurons. The distributions for transient visual indices (Cramer-von Mises test: $p < 3 \times 10^{-3}$) and transient popout indices (Cramer-von Mises test: $p < 1.3 \times 10^{-2}$) were significantly greater for short τ neurons compared to the long τ neurons. In contrast, sustained indices were not significantly different for either visual (Cramer-von Mises test: $p = 0.16$) or popout (Cramer-von Mises test: $p = 0.96$) at the individual level (Fig. 3C). Additionally, the visual onsets for the two groups did not significantly differ from each other for single (Cramer-von Mises test: $p = 0.19$) or popout stimuli (Cramer-von Mises test: $p = 0.08$) (Fig. S7A). These findings align with the results from the regression analyses, demonstrating that neurons with shorter timescales exhibit stronger, but not faster, transient visual responses and attentional modulation.

Next, we compared the amount of visual and attentional information that short and long τ neurons had at the population level and performed pseudo-population decoding analysis to predict the location of a single stimulus inside or outside the RFs (visual-decoding) and the location of popout stimulus inside or outside the RFs (popout-decoding) (Methods). We generated neuron-dropping curves (NDCs; Lebedev, 2014; Pettine et al., 2019; Wessberg et al., 2000) using the

performance of neuronal subsets obtained from either short or long τ neurons to examine decoding accuracies across varying population sizes. Both groups had high decoding accuracy, consistently above chance level across all population sizes, but differed in their performance profiles (Fig. 3D-E).

To quantify their differences in decoding performance, we calculated the area under the curve (AUC) exceeding the chance level for each group to assess population decoding performance (Fig. 3F; complementary findings from the saturation fitting analysis are also available in Fig. S3). Both visual- and popout-decoding performances differed significantly between short and long τ neurons across both transient and sustained periods. Short τ neurons exhibited higher AUC values for visual-decoding during the transient period (Wilcoxon rank-sum test: $p = 2.83 \times 10^{-13}$, effect size = 0.60; median = 0.995 for short τ vs. 0.993 for long τ). In comparison, long τ neurons exhibited better visual-decoding performance during the sustained period (Wilcoxon rank-sum test: $p = 8.41 \times 10^{-3}$, effect size = 0.22; median = 0.979 for long τ vs. 0.976 for short τ). Additionally, long τ neurons had a greater popout-decoding performance during both the transient (Wilcoxon rank-sum test: $p = 1.49 \times 10^{-2}$, effect size = 0.20; median = 0.818 for long τ vs. 0.810 for short τ) and sustained periods (Wilcoxon rank-sum test: $p = 1.98 \times 10^{-5}$, effect size = 0.35; median = 0.880 for long τ vs. 0.868 for short τ). The differences between the groups were most pronounced for visual-decoding in the transient period (effect size = 0.60) and popout-decoding in the sustained period (effect size = 0.35). These results highlight the complementary roles of short and long τ neurons in visual and attentional modulation, with short τ neurons specialized for short-lived, transient visual responses and long τ neurons for sustained attentional modulation.

In summary, intrinsic neural timescales in the FEF are closely linked to visual response and attentional modulation at both the individual and population levels, with short τ neurons excelling in transient visual processing and long τ neurons playing a greater role in sustained attentional modulation.

PPC inactivation slows intrinsic neuronal dynamics in FEF neurons

We then investigated the effects of PPC inactivation on the FEF intrinsic timescales to understand how PPC regulates local neuronal dynamics within the FEF. PPC inactivation was achieved using cryoloops implanted in IPS, which suppressed neuronal activity by lowering the temperature of the cortical tissue. The effectiveness of PPC inactivation was confirmed by robust behavioral effects in both the free viewing task and the double-target choice task during inactivation (Chen et al., 2020). Similar to the control condition, the exponential function showed a good fit to each neuron's autocorrelation profiles during the inactivation (mean R-squared = 0.8; Monkey J = 0.75; Monkey Q = 0.84; Fig. 1SB). Figure 4A shows six representative neurons, illustrating the changes in their timescales during PPC inactivation. These neurons exhibited an increase in their intrinsic timescales, reflecting slower dynamics and a more stable firing pattern during the baseline period. Consistently, we found a significant increase in intrinsic timescales across the entire population of FEF neurons following PPC inactivation (Wilcoxon signed-rank test: $p = 5.09 \times 10^{-13}$, effect size = 0.432, mean = 84.43 ms, median = 94.92 ms for inactivation vs. mean = 69.89 ms, median = 73.14 ms for control) (Fig. 4B). This increase in intrinsic neural timescales was evident for both monkeys (Wilcoxon signed-rank test: $p = 3.02 \times 10^{-2}$, effect size = 0.19 for Monkey J; $p = 4 \times 10^{-15}$, effect size = 0.63 for Monkey Q). Thus, PPC inactivation robustly slowed neuronal dynamics across FEF neurons.

We further examined the impact of PPC inactivation at the population level using the neuron-dropping curves (Fig. 5C-D). Consistent with individual neurons, PPC inactivation had a larger impact on stimulus-driven attention modulation than visual response and a larger impact on long

τ neurons compared to short τ neurons (Fig. 5E-F). Specifically, for visual-decoding performance, both short and long τ neurons showed slight but significant decreases in AUC above the chance level during the transient period. Short τ neurons decreased by 0.31% (Wilcoxon signed-rank test: $p = 4.64 \times 10^{-12}$) and long τ neurons decreased by 0.67% (Wilcoxon signed-rank test: $p = 8.46 \times 10^{-16}$), with long τ neurons exhibiting a larger reduction (Wilcoxon rank-sum test: $p = 5.94 \times 10^{-8}$). During the sustained period, the decreases were 0.31% for short τ (Wilcoxon signed-rank test: $p = 1.12 \times 10^{-3}$) and 1.97% for long τ (Wilcoxon signed-rank test: $p = 9.46 \times 10^{-18}$), again showing a more pronounced decline in long τ neurons (Wilcoxon rank-sum test: $p = 1.01 \times 10^{-20}$). In contrast, popout-decoding performance exhibited more substantial declines. Short τ neurons experienced a 21.50% decrease in transient popout-decoding performance (Wilcoxon signed-rank test: $p = 3.96 \times 10^{-18}$) and a 12.84% reduction in sustained popout-decoding performance (Wilcoxon signed-rank test: $p = 3.96 \times 10^{-18}$), while long τ neurons showed a 20.07% drop in transient popout-decoding performance (Wilcoxon signed-rank test: $p = 3.96 \times 10^{-18}$) and a 23.28% decrease in sustained popout-decoding performance (Wilcoxon signed-rank test: $p = 3.96 \times 10^{-18}$). Although both groups exhibited reductions, long τ neurons demonstrated a significantly greater decrease for the popout-decoding performance in the sustained period (Wilcoxon rank-sum test: $p = 1.23 \times 10^{-28}$) (Fig. 5E-F). Similar results can be observed by comparing the saturation rate and asymptote of NDCs across control and inactivation conditions (Fig. S5).

PPC inactivation selectively weakened the stimulus-driven attentional modulation in FEF neurons

Finally, we assessed the effects of PPC inactivation on stimulus-driven attention. We first analyzed the relationship between neural timescales and the functional properties of FEF neurons during PPC inactivation. Similar to the control condition, we employed multiple linear regression analysis to assess the correlation between intrinsic neural timescales and both visual and popout indices during inactivation condition (Fig. 5A and S4). Our results revealed that the correlation between intrinsic timescales and attentional modulation relies on the input from PPC during both transient and sustained periods. Specifically, the significant negative association between transient popout and intrinsic timescales in the control condition (Permutation test: $p = 2.05 \times 10^{-2}$, $\beta = -53.98$) was no longer significant during PPC inactivation (Permutation test: $p = 0.63$, $\beta = -12.45$). Additionally, the positive association between sustained popout indices and intrinsic timescales under control conditions (Permutation test: $p = 9 \times 10^{-4}$, $\beta = 77.18$) became non-significant following inactivation (Permutation test: $p = 0.21$, $\beta = -32.12$). In contrast, for visual modulation, PPC inactivation reduced but did not eliminate the significant negative correlation between intrinsic timescales and transient visual indices (Permutation test: $p = 2 \times 10^{-4}$, $\beta = -73.98$ under control; $p = 2.53 \times 10^{-2}$, $\beta = -44.83$ after inactivation). In contrast, no significant relationship was found between intrinsic timescales and sustained visual indices in either condition (Permutation test: $p = 0.24$, $\beta = 26.32$ under control; $p = 0.54$, $\beta = 13.77$ after inactivation). Thus, PPC inactivation has a larger impact on the correlation between neural timescales and attentional modulation compared to visual response.

We next compared the impact of PPC inactivation on visual response and attentional modulation, and asked whether the effect differs between short and long τ neurons. We quantified the impact of PPC inactivation for each individual neuron using the changes in visual and popout indices. Consistent with the linear regression analysis and our previous findings (Chen et al., 2020), PPC inactivation had a significantly larger impact on popout indices than visual indices during the sustained period (Wilcoxon rank-sum test: $p = 2.17 \times 10^{-4}$). Specifically, it had a greater effect on long τ neurons, affecting the transient visual (Cramér-von Mises test:

$p = 1.70 \times 10^{-2}$) and the sustained popout indices (Cramér-von Mises test: $p < 10^{-2}$) (Fig. 5B). Additionally, the visual onsets of the two groups were significantly delayed following PPC inactivation for both single (Cramér-von Mises test: $p = 7 \times 10^{-3}$ for short τ and $p < 10^{-3}$ for long τ) and popout stimuli (Cramér-von Mises test: $p < 10^{-3}$ for short τ and $p = 1.3 \times 10^{-2}$ for long τ) (Fig. S7B-C).

We further examined the impact of PPC inactivation at the population level using the neuron-dropping curves (Fig. 5C-D). Consistent with individual neurons, PPC inactivation had a larger impact on stimulus-driven attention modulation than visual response and a larger impact on long τ neurons compared to short τ neurons (Fig. 5E-F). Specifically, for visual-decoding performance, both short and long τ neurons showed slight but significant decreases in AUC above the chance level during the transient period (-0.31% for short τ, Δ: Wilcoxon signed-rank test: $p = 4.64 \times 10^{-12}$; -0.67% for long τ, Δ: Wilcoxon signed-rank test: $p = 8.46 \times 10^{-16}$), with long τ neurons exhibiting a larger reduction (Δ: Wilcoxon rank-sum test: $p = 5.94 \times 10^{-8}$). During the sustained period, the decreases were -0.31% for short τ (Δ: Wilcoxon signed-rank test: $p = 1.12 \times 10^{-3}$) and -1.97% for long τ (Δ: Wilcoxon signed-rank test: $p = 9.46 \times 10^{-18}$), again showing a more pronounced decline in long τ neurons (Δ: Wilcoxon rank-sum test: $p = 1.01 \times 10^{-20}$). In contrast, popout-decoding performance exhibited more substantial declines. Short τ neurons experienced a 21.50% decrease in transient popout-decoding performance (Δ: Wilcoxon signed-rank test: $p = 3.96 \times 10^{-18}$) and a 12.84% reduction in sustained popout-decoding performance (Δ: Wilcoxon signed-rank test: $p = 3.96 \times 10^{-18}$), while long τ neurons showed a 20.07% drop in transient popout-decoding performance (Δ: Wilcoxon signed-rank test: $p = 3.96 \times 10^{-18}$) and a 23.28% decrease in sustained popout-decoding performance (Δ: Wilcoxon signed-rank test: $p = 3.96 \times 10^{-18}$). Although both groups exhibited reductions, long τ neurons demonstrated a significantly greater decrease for the popout-decoding performance in the sustained period (Δ: Wilcoxon rank-sum test: $p = 1.23 \times 10^{-28}$) (Fig. 5E-F). Similar results can be observed by comparing the saturation rate and asymptote of NDCs across control and inactivation conditions (Fig. S5).

In summary, PPC inactivation disrupted the relationship between intrinsic neural timescales and stimulus-driven attentional modulation, eliminating significant correlations with both transient and sustained pop-out indices. At the individual neuronal level, PPC inactivation largely affected long τ neurons, impairing both their visual responses and attention modulation, particularly during the sustained attention period. At the population level, PPC inactivation led to significant declines in decoding performance for both visual target detection and attentional modulation, with long τ neurons being most impacted during sustained attentional modulation.

Discussion

We found that intrinsic neural timescales within the FEF exhibited a bimodal distribution, distinguishing two distinct neuronal populations with fast and slow intrinsic neuronal dynamics. These timescales, measured during the task-free passive fixation period, were correlated with the neurons' visual responses and stimulus-driven attentional modulation during the task. Specifically, short τ neurons were predominantly involved in transient visual processing, exhibiting greater transient responses to visual stimuli. In contrast, long τ neurons showed stronger sustained attentional modulation. Notably, PPC inactivation selectively increased the intrinsic timescales of short τ neurons during the task-free period, while diminishing stimulus-driven attentional modulation in long τ neurons. These findings provide the first causal evidence for the critical role of PPC in regulating intrinsic neuronal dynamics and stimulus-driven attentional modulation in the FEF and suggest context-dependent roles of PPC input in influencing FEF activity.

Our observations provide important evidence suggesting that there are two distinct neuronal

populations of FEF neurons with fast and slow dynamics. This distinction was supported by the consistent bimodal distribution of intrinsic neural timescales observed for each individual monkey. In addition, this differentiation was further supported by the fact that PPC inactivation had selective impacts on intrinsic timescales of short τ neurons and task responses of long τ neurons. These heterogeneities in intrinsic timescales may offer computational advantages in supporting the diverse role of FEF in behavior and cognitive functions, including visually guided saccade movements (Bruce and Goldberg, 1985; Dias and Segraves, 1999), visual-spatial attention (Hüer et al., 2024; Moore and Fallah, 2001, 2004; Thompson et al., 2005), decision-making (Ding and Gold, 2012) and working memory (Armstrong et al., 2009; Clark et al., 2012; Hasegawa et al., 2004). Short τ neurons may enable rapid updates and responses to dynamic environments, while long τ neurons facilitate information integration over time and visual space, supporting the identification of salient stimuli within the visual field and maintaining this information over a sustained period (Itti and Koch, 2001). The coexistence of these two network motifs may allow FEF neurons to flexibly prioritize neural populations with slower or faster dynamics, allowing them to adapt to varying task demands (Cavanagh et al., 2020).

Different functional and anatomical classes of FEF neurons may exhibit different intrinsic timescales. However, it remains unclear how the heterogeneity of intrinsic timescales maps onto these classes. FEF neurons have traditionally been classified into visual neurons, motor neurons, visuomotor neurons, and memory-delay neurons, based on their functional properties (Bruce and Goldberg, 1985; Thompson et al., 2005). Visual neurons likely have shorter timescales, given their strong visual responses. Memory-delayed neurons, on the other hand, exhibit longer timescales as reported in previous studies (Wasmuht et al., 2018). In addition to stimulus-driven attention, these long τ neurons may also play a dominant role in goal-directed attention deployment, modulating activity in the visual cortex via their direct axonal projections (Hüer et al., 2024; Merrikhi et al., 2017). Furthermore, the laminar organization of the FEF likely contributes to the diversity in these timescales (Heinzle et al., 2007). Neurons in granular layers predominantly receive feedforward visual input. These neurons show higher visual sensitivity (Chen et al., 2018) and may exhibit shorter timescales. In contrast, neurons in super- and infragranular layers are likely involved in feedback and integrative functions, and may exhibit longer timescales. Additionally, inhibitory and excitatory neurons may differ in their intrinsic timescales (Cavanagh et al., 2020). However, short and long τ neurons are unlikely to directly map to the inhibitory and excitatory neuron classes, as the ratio of the short and long τ neurons is approximately 4:5, whereas the ratio of excitatory versus inhibitory neurons in FEF is closer to 4:1 (Heinzle et al., 2007). Future research is needed to further explore these relationships.

The impact of PPC inactivation appears to be context-dependent. Specifically, PPC inactivation has approximately a 15-fold greater impact on the modulation of intrinsic timescales in short τ neurons during the baseline period and at least 2-fold greater impact on attentional modulation in long τ neurons during the task period. These findings suggest that these two neuronal populations may rely on distinct circuit connections. We hypothesize the presence of at least two network motifs, each contributed by short τ and long τ neurons (Fig. 6). Short τ neurons exhibit strong transient visual and weak attentional modulation, indicating their role in relaying visual input while being less involved in stimulus competition. These neurons are likely feedforward recipients, receiving direct projections from the PPC and other posterior visual regions, such as those in the occipital lobes (Schall et al., 1995; Stanton et al., 1995). They may have weaker recurrent connections with themselves and other PFC neurons. Therefore, PPC inactivation has a stronger impact on their intrinsic dynamics, as feedforward connections dominate their network connections. In addition, their visual responses are likely less affected due to compensatory input from other visual regions, such as primary and extrastriate visual cortices (Fig. 6A). In contrast, long τ neurons exhibit robust attentional modulation, reflecting their role in stimulus competition during stimulus-driven attention. PPC input serves as the primary source of

visual and attentional input for these neurons (Fig. 6B). Specifically, the input from PPC or reciprocal connections between PPC and FEF may play an important role in salience computation (Buschman and Miller, 2007; Chen et al., 2020; Constantinidis and Steinmetz, 2005), especially maintaining attentional modulation during the sustained period. Anatomically, these neurons may have stronger recurrent connections within the PFC that support their sustained activity and dominate their intrinsic dynamics. As a result, PPC inactivation has a weaker effect on their intrinsic dynamics and a greater impact on their visual and attentional modulation. Future studies with large-scale recordings across both PPC and FEF are essential to uncover the detailed circuit connections underlying these FEF neurons.

Lastly, the present results provide direct evidence of PPC in modulating intrinsic timescales of FEF neurons. Previous computational models suggest that intrinsic timescales arise from a combination of diverse excitatory connection strengths across different regions and long-range connectivity patterns, indicating that neither factor alone is sufficient to predict a region's timescales (Chaudhuri et al., 2014, 2015; Litwin-Kumar and Doiron, 2012). However, the causal role of intra-area connections and long-range connectivity patterns in modulating intrinsic timescales has not yet been tested. Here, we provide the first empirical evidence supporting computational models linking intrinsic timescales to network connectivity. Specifically, the modulation of FEF intrinsic timescales by PPC inputs demonstrates a dependence of FEF temporal properties on long-range connectivity. We hypothesize that this slower FEF dynamic during PPC inactivation may result from either or both of the two factors. First, FEF neurons are known to have slower timescales than PPC neurons (Murray et al., 2014; Wasmuht et al., 2018). During PPC inactivation, the removal of input from faster-dynamic PPC neurons may unmask slower local FEF timescales, leading to an overall increase in the intrinsic timescales of FEF neurons (Chaudhuri et al., 2015). Second, the slower timescale may also reflect the recruitment of FEF neurons by stronger recurrent structures within the FEF or prefrontal cortex during PPC inactivation (Litwin-Kumar and Doiron, 2012). Future studies combining high-density recordings with targeted manipulation will be critical to test these hypotheses.

Methods

Subject details

All experimental procedures followed the guidelines set by the National Institutes of Health Guide for the Care and Use of Laboratory Animals, the Society for Neuroscience Guidelines and Policies, and the Stanford University Animal Care and Use Committee. The experiments involved two healthy male rhesus macaques (Macaca mulatta): monkey Q (16 kg) and monkey J (17 kg). The number of animals used aligns with typical practices for neurophysiological studies involving non-human primates.

Experimental procedures

The details of the surgical procedures and neurophysiological recordings have been previously reported by (Chen et al., 2020). In summary, two monkeys (Q, 16 kg; J, 17 kg) performed visual sensitivity and saliency-driven attention tasks under PPC-inactivation and control conditions while we monitored neural activity in the FEF (Fig. 1A). Each trial began with an initial central fixation period (1×1 dva) of 500 ms on a gray background (60 cd/m^2), with the last 300 ms serving as the baseline period. Following this, the monkeys were presented with either a single stimulus or a popout stimulus for 500 ms while continuing to fixate at the center (Fig. 1B). In the single stimulus trials, a red or green square stimulus (7×7 dva) was displayed at one of 24 locations on a 6×4 grid (75×45 dva). In the popout trials, a square stimulus was placed among an array of stimuli with contrasting colors (e.g., a red square among green stimuli or a green square among red stimuli). After the stimulus offset, the monkeys continued to fixate for an additional 500 ms to receive a reward (Fig. 1C).

Neurophysiological recording of FEF neurons

The recording locations within the right FEF were identified by eliciting short-latency saccadic eye movements using biphasic current pulses ($\leq$ 50 µA; 250 Hz; 0.25 ms duration), in line with methods from previous studies (Bruce et al., 1985). Neural activity was recorded using 16 or 32-channel linear array electrodes (V and S-Probes, Plexon, Inc.), with contacts spaced 150 µm apart. These electrodes were inserted into the cortex via a hydraulic microdrive (Narishige International). Neural signals were referenced to a nearby stainless steel guide tube positioned near the electrode contacts. The signal used for spike detection was filtered with a 4-pole Bessel high-pass filter at 300 Hz and a 2-pole Bessel low-pass filter at 6000 Hz, and sampled at 40 kHz. Initial classification of extracellular waveforms into single neurons or multi-units was performed online via template matching, with offline sorting subsequently verified using Plexon systems. In total, we recorded spike timestamps from 400 neural units in the FEF across the two monkeys.

Reversible inactivation of PPC

In each monkey, a pair of stainless steel cryoloops was implanted in the intraparietal sulcus (IPS) of the right hemisphere. These cryoloops were custom-designed to fit the contours of the IPS and fill the sulcus. The IPS was cooled by circulating chilled methanol through the loop tubing, with the temperature closely monitored and maintained within 1 ℃ of the target value by adjusting the methanol flow rate. A stable loop temperature of approximately 5 ℃ was reached within 5–10 minutes after the cooling process began, and the brain's normal temperature was restored within about 2 minutes post-cooling. Temperatures around 5 ℃ in the loop have been shown to effectively suppress neuronal activity in the underlying cortex (Lomber and Payne, 2000). During

the experimental sessions, inactivation periods lasted 30 to 60 minutes each. Neurophysiological data were first collected during a control block, followed by an inactivation block across eight sessions. In six additional sessions, data collection followed two consecutive sets of control and inactivation phases (control-inactivation-control-inactivation), allowing the examination of potential block order effects. The success of PPC inactivation on behavior was evaluated in separate sessions using double-target choice tasks and free viewing of natural images (Chen et al., 2020).

Computation of intrinsic neural timescales

We analyzed neural activity from 400 neural units in the FEF across two monkeys. Each unit's activity was recorded as spike timestamps, which were binned into 10 ms intervals to calculate spike counts for each trial. To normalize the spike counts at each time bin across all trials, we subtracted the mean firing rate of each time bin from the spike count in that bin. This step helped isolate the intrinsic temporal dependencies of the neuron's firing pattern, independent of its overall firing rate. We then performed autocorrelation analysis on the 300 ms baseline windows of each trial to compute the sum of products of spike count values against themselves at various lags for each neuron. The autocorrelation values for each lag were first averaged across trials for each neuron. Next, these averaged autocorrelation values were scaled by dividing them by the zero-lag value, standardizing the results for each neuron.

We then fitted a single exponential decay function to these averaged autocorrelation values and calculated the decay time constants for each neuron, representing their intrinsic neural timescales (Fig. 1D). Importantly, a subset of neurons displayed significantly low autocorrelation values at short time lags, suggesting the presence of refractory periods or negative adaptation, as reported in previous studies (Cavanagh et al., 2016; Murray et al., 2014; Wasmuht et al., 2018). Therefore, the fitting procedure was started at the time lag—excluding the zeroth lag where autocorrelation equals one—where the mean autocorrelation reached its maximum value. For the curve fitting, we used the Trust Region Reflective algorithm. The model used for the fitting process is given by the equation:

$$f(x) = A \cdot \left(e^{-\frac{x}{\tau}} + B\right) \tag{1}$$

where x is the time lag, τ represents the intrinsic timescale, A is the amplitude of the decay, and B is included to adjust for baseline shifts, addressing the influence of intrinsic neural timescales that extend beyond the measurement window.

To establish an objective criterion for the goodness of fit, we calculated pseudo-R-squared values for nonlinear fitting based on the proportion of the total variance explained by the exponential decay function. We found that 5% of units had pseudo-R-squared values below 0.3, indicating a poor fit. Additionally, 6.5% of units fell within the range of 0.3 to 0.5, representing a moderate fit, and 13% of units had values between 0.5 and 0.7, suggesting a good fit. The majority, 75.5% of units, demonstrated values ranging from 0.7 to 1.0, indicating an excellent model fit (Fig. S1). Neurons with pseudo-R-squared values below 0.3 were excluded from further analysis, resulting in a remaining sample of 380 neural units for the control condition and 372 neural units for the inactivation condition.

Mode testing of intrinsic neural timescales

To investigate the distribution of intrinsic neural timescales in the FEF, we applied several statistical tests using the mode test function from the multimode R package (Ameijeiras-Alonso et al., 2021). Each test was chosen for its ability to highlight different aspects of distribution modality. We used the Hall and York Critical Bandwidth Test (Hall and York, 2001), which refines bandwidth

selection in kernel density estimation to improve the detection of subtle multimodal patterns. The Fisher and Marron Cramer-von Mises Test (Fisher and Marron, 2001) was applied for its sensitivity in capturing subtle features like shoulder modes by assessing how well the empirical distribution function fits a hypothesized unimodal function using the Cramer-von Mises statistic. Additionally, we used the Ameijeiras-Alonso et al. Excess Mass Test (Ameijeiras-Alonso et al., 2019), which employs the excess mass criterion for mode detection, offering a robust method particularly suited for multidimensional datasets with high noise levels. All tests provided complementary results (Table S1).

Calculation of visual and popout indices

We measured the receptive field of each neuron by analyzing their neural responses to a single stimulus presented in each of 24 locations. For those locations where a neuron's firing rate exceeded 95% of its maximum response, we included them within the neuron's receptive field. In contrast, the four locations in the far-right column of the ipsilateral visual field were considered outside the receptive field. Following this, we computed visual indices for each neuron, reflecting the neural activity during transient (50–200 ms) and sustained (200–500 ms) periods for both single and popout stimulus trials. These indices were calculated based on the average differential spike rate when stimuli were presented within versus outside the neuron's receptive field (In-RF vs. Out-RF; Fig. 1B), normalized by their sum.

$$\text{Visual index}_{i,\text{type, period}} = \frac{\overline{\text{In-RF}}_{i,\text{type, period}} - \overline{\text{Out-RF}}_{i,\text{type, period}}}{\overline{\text{In-RF}}_{i,\text{type, period}} + \overline{\text{Out-RF}}_{i,\text{type, period}}} \tag{2}$$

Here, i represents each neuron, 'type' refers to single or popout trials, and 'period' denotes transient or sustained periods. We computed four visual and popout indices corresponding to transient and sustained visual responses as well as attentional modulation. The distributions of visual and popout indices in the short and long τ neurons were compared using the Cramer-von Mises test (Fig. 3C).

Analyzing visual onsets

We quantified the earliest time at which each neuron's activity rose significantly above baseline, separately for single and popout trials. Specifically, we computed the mean spike count for each 10 ms bin across trials. A baseline threshold was then defined by adding two standard deviations to the average spike count during the pre-stimulus window. Within the post-stimulus period, we then identified the first occurrence of at least two consecutive bins (20 ms) exceeding this threshold. The leading bin in this sequence was determined as the neuron's onset bin. By applying this procedure independently to single-stimulus and popout conditions, we observed that 92% of short τ neurons and 82% of long τ neurons showed a detectable onset under single-stimulus trials. Additionally, 86% of short τ neurons and 67% of long τ neurons displayed a detectable onset under popout trials. These results provided onset latencies that characterized the timing of visually evoked responses across stimulus conditions. Visual inspection of the neuronal activity traces confirmed the accuracy of these onset calculations. Similar results were observed when applying more stringent criteria.

Multiple linear regression analyses

We conducted multiple regression analyses to assess the individual contributions of each variable while accounting for their interdependencies. In our model, the dependent variable was the

intrinsic neural timescales, while the independent variables included the visual indices, popout indices, and the baseline mean firing rate. The regression model was specified as:

$$\tau_i = \beta_0 + \beta_1 \cdot \mathsf{V}_{t,i} + \beta_2 \cdot \mathsf{V}_{s,i} + \beta_3 \cdot \mathsf{A}_{t,i} + \beta_4 \cdot \mathsf{A}_{s,i} + \beta_5 \cdot \mathsf{F}_{b,i} + \epsilon_i \tag{3}$$

In this equation, $\tau_{b,i}$ denotes the intrinsic neural timescales for neuron i; $V_{t,i}$ and $V_{s,i}$ are the visual transient and sustained indices; $A_{t,i}$ and $A_{s,i}$ are the transient and sustained popout (stimulus-driven attention) indices; $F_{b,i}$ represents the baseline mean firing rate; and ϵ_i accounts for unexplained variance.

To fit the linear model, we used robust regression, which minimizes the influence of outliers and is less sensitive to non-normality in the data. This approach ensures that the coefficients accurately reflect the effect of each predictor on the dependent variable without being disproportionately influenced by outliers. We utilized added-variable plots to illustrate the relationship between neural timescales and each predictor by plotting the controlled residuals against each independent variable (Fig. 3A). These plots provide a visual representation of the distinct contributions of each predictor to the model, with the slopes quantifying the effect of a one-unit change in each predictor on the timescales while holding the other variables constant.

We checked for multicollinearity among the independent variables in the multiple regression model using Variance Inflation Factor (VIF) analysis. The VIF quantifies the degree to which the variance of a regression coefficient is inflated due to linear dependence on other predictors in the model. Generally, a VIF value greater than 5 or 10 suggests problematic multicollinearity (James et al., 2021), indicating that the affected predictors may be linearly dependent on others. In our analysis, we did not find significant multicollinearity (Fig. S2A).

Additionally, we examined the normality of the residuals in our model. A Q-Q plot was used to visually assess the distribution of residuals from our robust regression model against a theoretical normal distribution (Fig. S2B). Deviations from the line in this plot indicate departures from normality, suggesting that the residuals were not normally distributed. To address this, we used permutation testing to assess the significance of the regression coefficients. We employed a custom function to randomly shuffle the dependent variable, neural timescales, 10000 times while keeping the independent variables unchanged. This generated a distribution of regression coefficients under the null hypothesis of no association (Fig. 3A). P-values were calculated as the proportion of permuted coefficients whose absolute values equaled or exceeded that of the observed coefficient.

Neuron-dropping decoding analyses

To assess whether short and long τ neurons differ in visual responses and attentional modulation at the population level, we conducted a neuron-dropping analysis (Lebedev, 2014). We tested the ability to decode spatial location (inside vs. outside the receptive field) during both transient and sustained stimulus presentations in both single and popout trials. In other words, we decoded whether the single or popout stimulus was in the receptive field during single and popout trials, respectively (Chen et al., 2020). Neurons with fewer than 20 trials were excluded, resulting in 143 neurons in the short τ group and 190 neurons in the long τ group.

To evaluate the decoding performance of varying neuron group sizes, we incrementally analyzed groups starting with three neurons and expanding up to 120 neurons. The maximum number of neurons was capped at 120 to avoid potential statistical validity issues that can arise when the subpopulation size approaches that of the fixed population (Lebedev, 2014). At each step, we randomly sampled the specified number of neurons 500 times to ensure robust performance estimates. For each decoding analysis (across 500 iterations at each step), we equalized the number of trials for In-RF and Out-RF conditions by randomly sampling an equal number of

trials from each condition. Next, we conducted principal component analysis (PCA) retaining the top three principal components. A support vector machine (SVM) classifier was then used for decoding. Decoding performances exhibited saturation curves as the number of neurons increased, indicating diminishing returns in performance improvement with additional neurons.

To assess differences in growth rates between short and long τ neurons, we fit a saturation function defined as:

$$f(x) = A \cdot e^{-B \cdot x} + C \tag{4}$$

Here, x represents the number of neurons, ranging from 1 to 120; A is the initial amplitude; B is the saturation rate; and C is the asymptote value of the function. This approach allowed us to model and compare the dynamics of decoding performance as a function of population size between the two groups. To improve fitting accuracy, we averaged the results of every five iterations, resulting in 100 averaged data points for each group over the incremental steps up to 120 neurons. The saturation function was then fitted to these averaged data points for each condition, and the parameters B and C were compared between short and long τ neurons using the nonparametric Wilcoxon rank-sum test (Fig. S3).

Additionally, we analyzed the area under the curve (AUC) for decoding performance. The AUC was calculated for each group based on the same 100 averaged data points, measuring the area above the chance level. This provided an overall measure of decoding performance across all population sizes. To standardize the results, we normalized the AUC by dividing it by the maximum possible area above chance. A normalized score of 0 indicates overall performance at the chance level, whereas a score of 1 reflects perfect decoding accuracy across all population sizes. The AUC was computed using the trapezoidal rule, which finds the area between consecutive points to determine overall decoding performance. The resulting normalized AUC scores were then compared between short and long τ neurons using the nonparametric Wilcoxon rank-sum test (Fig. 3).

Testing the effect of parietal inactivation

To investigate the effects of parietal inactivation on intrinsic neural timescales, visual responses, and attentional modulation in the FEF, we conducted a series of statistical analyses. First, we performed paired Wilcoxon signed-rank tests to determine whether parietal inactivation led to significant changes in FEF neural timescales, assessing the direction of change (increase or decrease) across both monkeys and within each individual monkey. The rank biserial correlation effect size was calculated to quantify the magnitude of the observed changes (Fig. 4B). Next, we analyzed whether the change (delta: inactivation - control) in neural timescales differed between short and long τ neurons. We first tested against zero using a one-sample Wilcoxon signed-rank test to determine whether the change within each group was significant, followed by unpaired Wilcoxon rank-sum tests to compare the magnitude of change between the two groups (Fig. 4E).

We also examined whether the relationships between neural timescales and visual/attentional responses observed in the control condition persisted or were altered during inactivation. A multiple regression analysis was conducted using values obtained after inactivation, with intrinsic neural timescales as the dependent variable and visual indices along with baseline firing rate as independent variables (Fig. 5A). Additionally, changes in the distribution of visual and popout indices were compared between short and long τ neurons using the Cramer-von Mises test (Fig. 5). Furthermore, we performed a neuron-dropping analysis (Lebedev, 2014) under PPC inactivation to evaluate changes in visual- and popout-decoding performance at the population level (Fig. 5C-D). The function parameters (saturation rate and asymptote value) were compared

between short and long τ neurons in both conditions (Fig. S5). Lastly, we compared changes in the normalized AUC scores between the two groups following PPC inactivation (Fig. 5E).

Data and code availability

The datasets and code supporting the current study have not been deposited in a public repository due to their volume and complexity but will be made available by the lead contact (X.C.) upon request.

Acknowledgments

This work was supported by the National Science Foundation National Research Traineeship (NSF NRT) under Grant No. 2152260 (to O.S.), National Institutes of Health grants EY014924 (to X.C.) and EY029759 (to T.M.), the Brain and Behavior Research Foundation (to X.C.), the Alfred P. Sloan Foundation under Grant No. FG-2021-16304 (to R.C.), and the UC Davis Large Interdisciplinary Applications in Neuroscience (LIAN) (to R.C. and X.C.).

Competing interests

The authors declare no competing interests.

Main Figure Titles And Legends

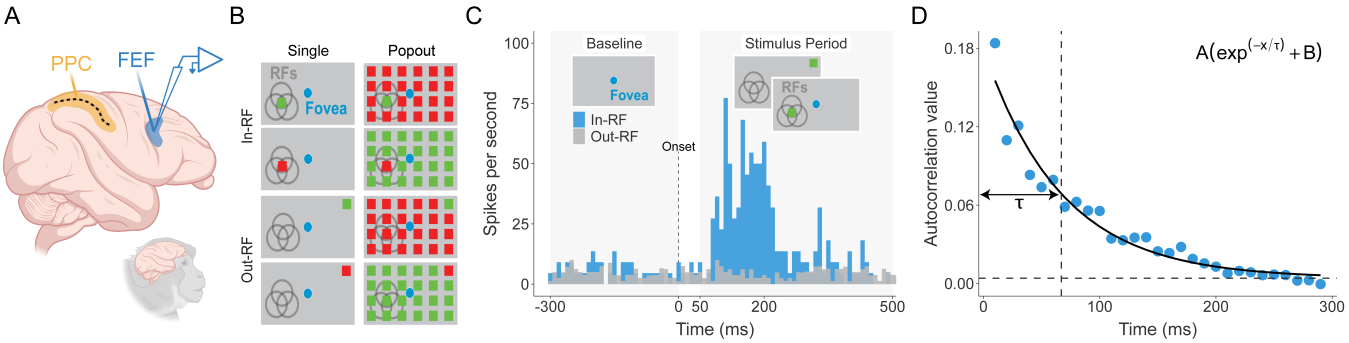

Fig. 1 | Experimental setup and intrinsic neural timescales.

(A) Recordings from the frontal eye field (FEF) were performed using a linear electrode array, both with and without inactivation of the posterior parietal cortex (PPC). (B) Visual stimuli consisted of a single-colored stimulus presented in isolation (Single) or among an array of identically colored stimuli (Popout). (C) Mean response of an example neuron to a single stimulus presented inside (blue) versus outside (gray) the receptive field (RF). (D) Spike-count autocorrelation was computed for neuronal spiking activity during the baseline period. Blue dots represent autocorrelation coefficients at different time lags. The decay rate of the autocorrelation profiles was quantified by fitting an exponential decay function with an offset. The resulting time constant (τ) represents the intrinsic neural timescale, measuring the rate at which autocorrelation decays over time.

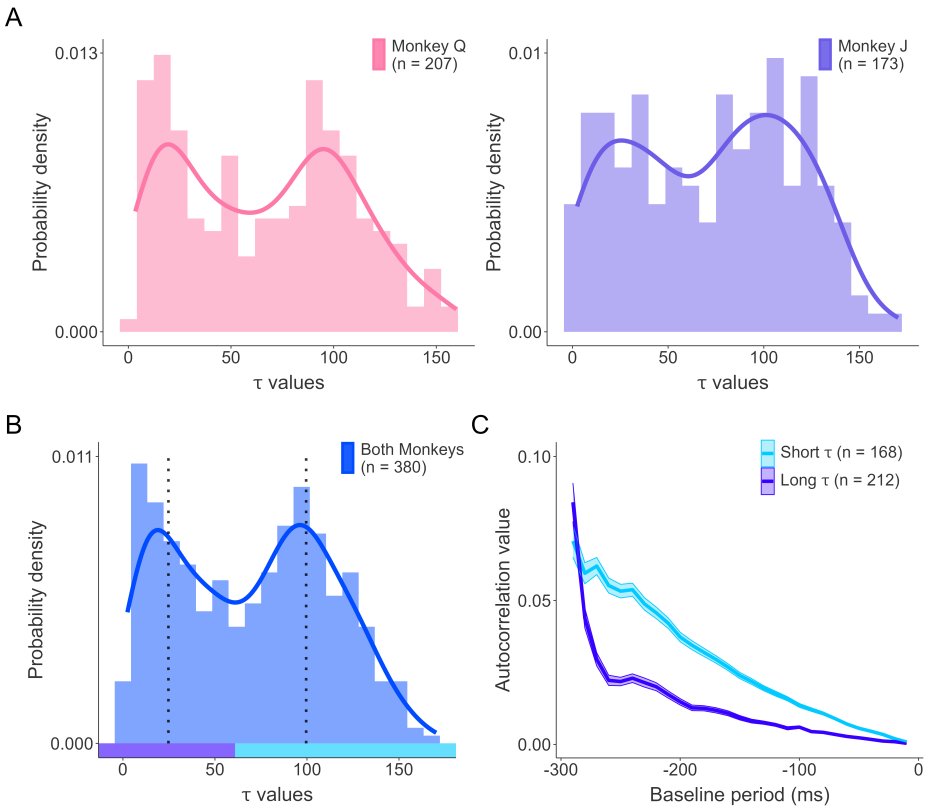

Fig. 2 | Distribution of intrinsic neural timescales in FEF neurons.

(A) The distributions of intrinsic neural timescales (τ) were significantly bimodal for both monkeys. Solid lines represent the kernel density functions, while dashed lines indicate the global minima used to categorize neurons into short-timescale (short τ) and long-timescale (long τ) groups. (B) Distribution of τ values along with their kernel density plots across both monkeys. Dotted lines denote the median for each group. (C) The averaged autocorrelation profiles for all the short τ (blue) and long τ (purple) neurons during the baseline period. Shaded areas indicate ± SEM at each time point.

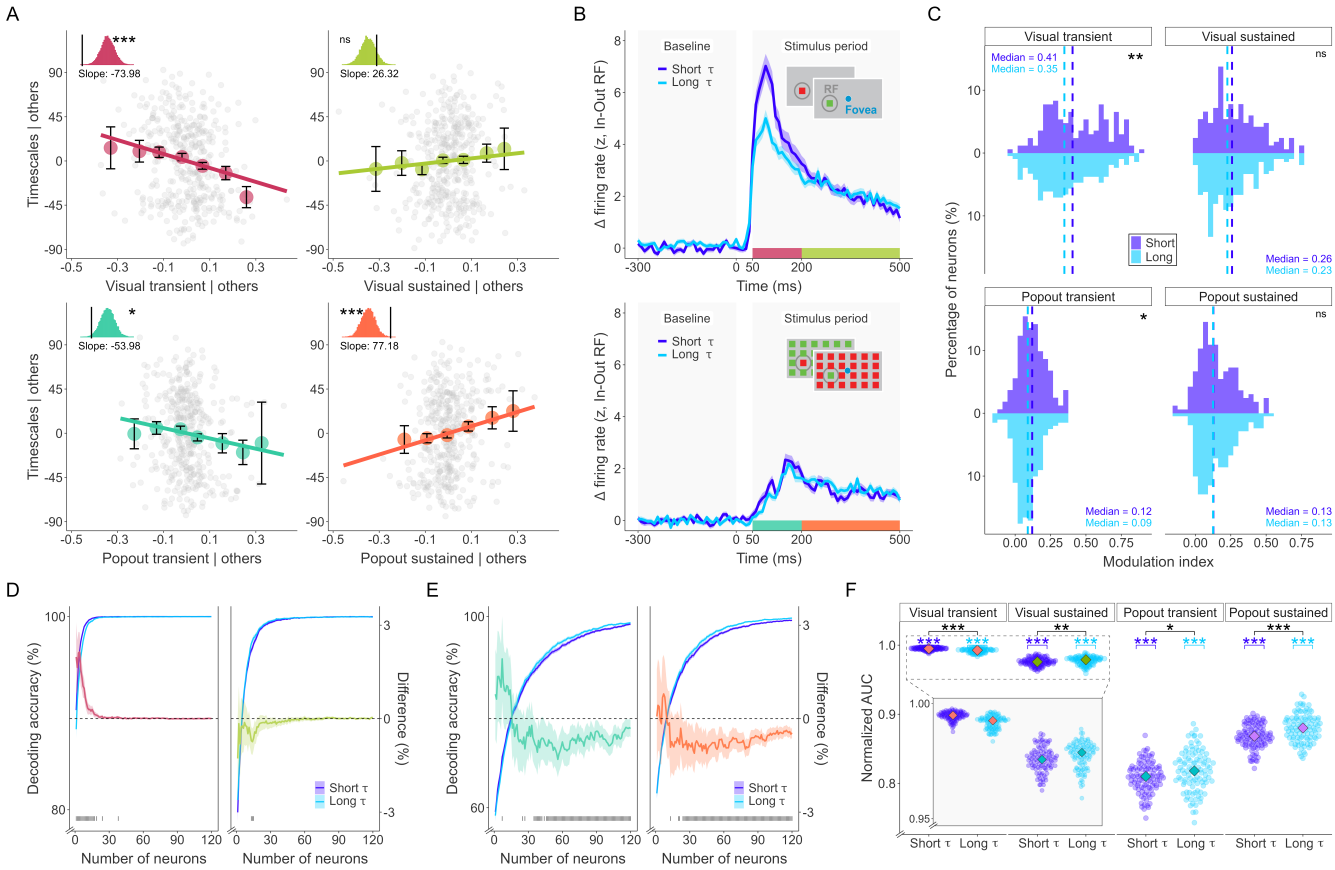

Fig. 3 | Relationship between intrinsic neural timescales and functional properties of FEF neurons.

(A) Added-variable plots showing the associations between intrinsic neural timescales and visual (top) and popout (bottom) indices. Insets display slopes and significance levels from nonparametric permutation tests. (B) Mean response differences between single (top) and unique (bottom) stimuli presented inside versus outside receptive fields for neurons in the short-timescale group (short τ; purple) and the long-timescale group (long τ; blue). Shaded areas indicate ± SEM. (C) Distributions of visual and popout indices during transient and sustained periods for short τ (purple) and long τ neurons (blue). Dashed lines indicate median values for each group. (D) Population decoding performance for visual modulation as a function of population size for short τ (purple) and long τ neurons (blue). Results are shown separately for transient (left) and sustained (right) periods. Purple and blue lines represent average decoding accuracy, while colored lines indicate differences between the two groups. Ribbons represent 95% confidence intervals. The black dashed line marks zero difference, and significant differences are indicated by gray vertical lines. (E) Population decoding performance for attentional modulation as a function of population size. Conventions are the same as in (D). (F) Normalized area under the curve (AUC) values comparing population decoding performance for short τ (purple) and long τ neurons (blue). Diamonds represent median values for each group. The inset shows the results for visual-decoding performance on a finer scale. ($p < 0.05$; *$p < 0.01$; **$p < 0.001$; ns = not significant).

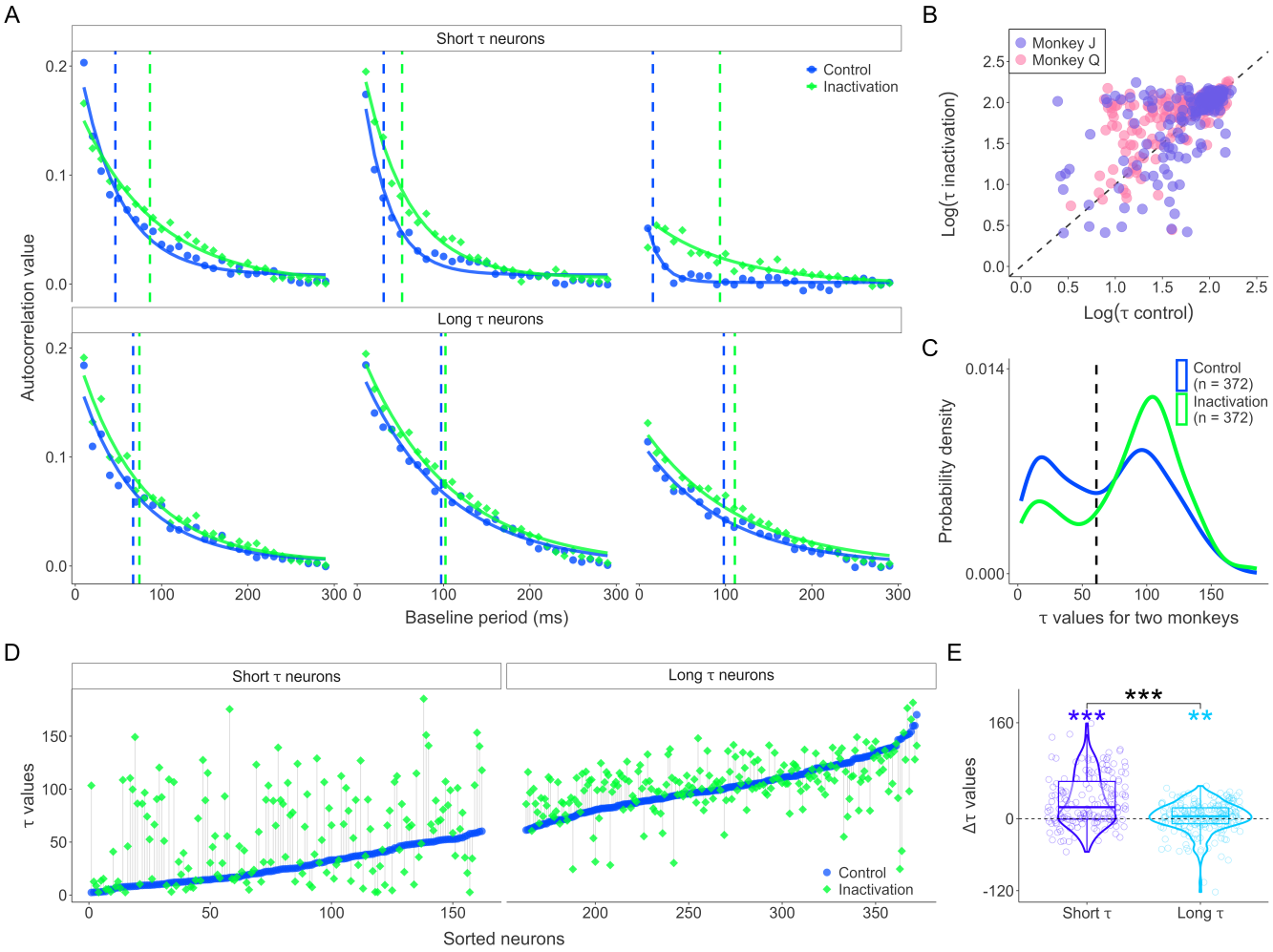

Fig. 4 | Effects of PPC inactivation on the intrinsic neural timescales of FEF neurons.

(A) Autocorrelation profiles of representative neurons with short timescales (short τ) (top) and long timescales (long τ) (bottom) during control (blue) and PPC inactivation (green). Dashed lines indicate the intrinsic neural timescale (τ) values for each condition. (B) Scatter plot of log-transformed τ values for control vs. inactivation conditions for both monkeys (purple: Monkey J; pink: Monkey Q). (C) Probability density plot of τ values for control and inactivation conditions across two monkeys. (D) τ values for short and long τ neurons in control and inactivation conditions. Neurons are sorted by their τ values during the control conditions. (E) Violin plots comparing the change in τ values between short and long τ neurons during PPC inactivation. (*** $p < 0.001$, ** $p < 0.01$, * $p < 0.05$, ns = not significant).

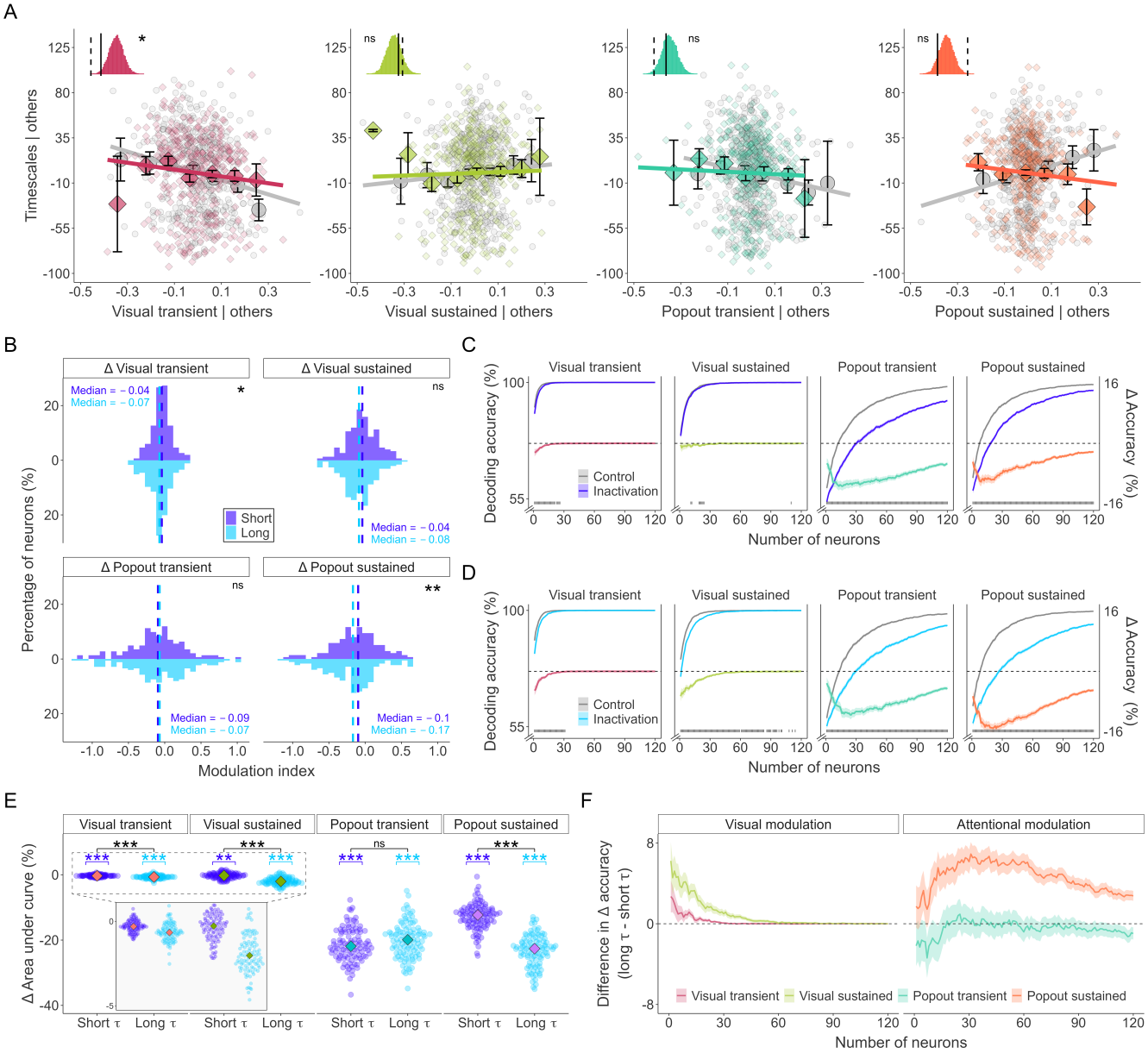

Fig. 5 | Effects of PPC inactivation on visual and attentional modulation in FEF neurons.

(A) Added-variable plots showing the relationship between intrinsic neural timescales and visual/popout indices before (gray circles) and after posterior parietal cortex (PPC) inactivation (colored diamonds). Insets display slopes and significance from permutation tests before (solid lines) and after inactivation (dashed lines). (B) Changes (Δ) in the distributions of visual and popout indices for the neurons in the short-timescale (short τ; purple) and long-timescale (long τ; blue) groups comparing control and PPC inactivation. Dashed lines indicate median changes. (C) Visual- and popout-decoding performances as a function of population size for short τ neurons under control (gray) and inactivation (purple) conditions. The figures correspond to visual transient, visual sustained, popout transient, and popout sustained periods from left to right. The secondary axis shows differences, with significant differences marked by gray vertical lines. (D) Same as (C), but for long τ neurons, with control (gray) and inactivation (blue) conditions. (E) Comparison of changes (Δ) in the area under the curve (AUC) for decoding performance be-

tween short τ and long τ neurons during PPC inactivation. Diamonds represent median values for each group. The inset shows the results for visual modulation on a finer scale. (F) Differences in Δ AUC between short τ and long τ neurons, with positive values indicating larger changes for long τ neurons and negative values indicating larger changes for short τ neurons ($p < 0.05$; *$p < 0.01$; **$p < 0.001$; ns = not significant).

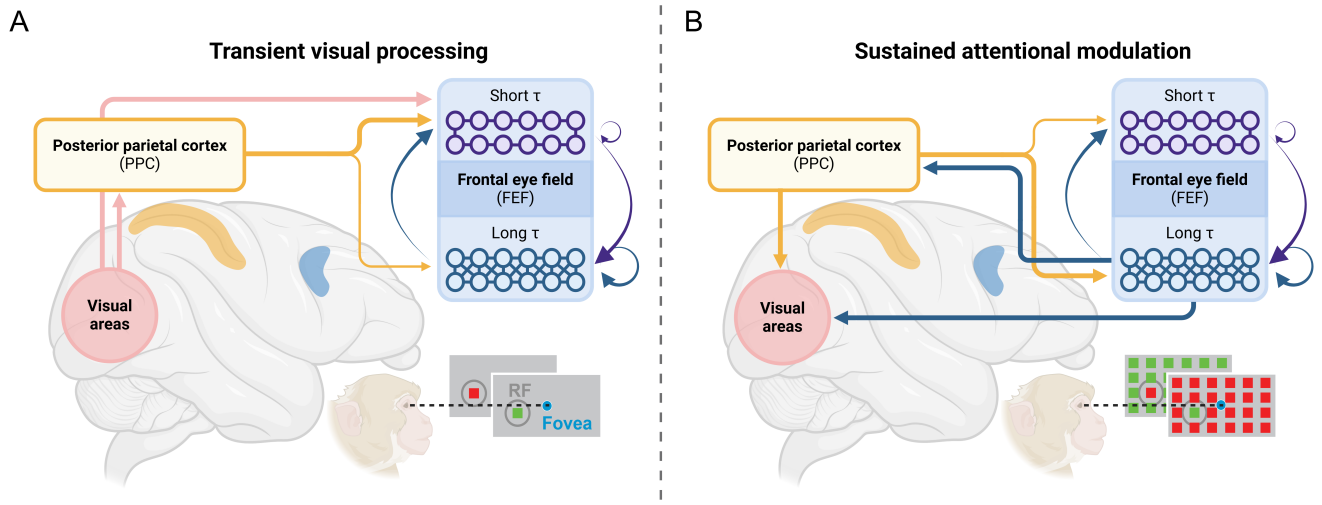

Fig. 6 | Proposed role of PPC during visual and attentional modulation in FEF.

(A) Transient visual processing: The frontal eye field (FEF) neurons in the short-timescale group (short τ) are hypothesized to be predominantly feedforward recipient neurons receiving projections from the posterior parietal cortex (PPC) and visual regions. These neurons exhibit relatively higher visual responses with lower attentional modulation, suggesting a primary role in relaying visual input. The intrinsic dynamics of short τ neurons are more affected by PPC inactivation due to their weaker recurrent connections. However, compensatory input from the visual cortex likely maintains their visual modulation. (B) Sustained attentional modulation: FEF neurons in the long-timescale group (long τ) are proposed to integrate substantial input from the PPC, particularly during the sustained attention period. These neurons exhibit stronger attentional modulation, reflecting their role in stimulus-driven attention. While PPC inactivation has a weaker effect on their intrinsic dynamics due to their robust recurrent connections within the prefrontal cortex, it significantly reduces their attentional modulation. This highlights PPC's critical role as their primary source of input for salience computation. Created in BioRender. Soyuhos, O. (2025) https://BioRender.com/g40r029.

References

Ameijeiras-Alonso, J., Crujeiras, R. M., and Rodriguez-Casal, A. (2021). multimode: An R Package for Mode Assessment. *Journal of Statistical Software*, 97:1–32.

Ameijeiras-Alonso, J., Crujeiras, R. M., and Rodríguez-Casal, A. (2019). Mode testing, critical bandwidth and excess mass. *TEST*, 28(3):900–919.

Anderson, J. C., Kennedy, H., and Martin, K. A. C. (2011). Pathways of Attention: Synaptic Relationships of Frontal Eye Field to V4, Lateral Intraparietal Cortex, and Area 46 in Macaque Monkey. *Journal of Neuroscience*, 31(30):10872–10881.

Armstrong, K. M., Chang, M. H., and Moore, T. (2009). Selection and Maintenance of Spatial Information by Frontal Eye Field Neurons. *Journal of Neuroscience*, 29(50):15621–15629.

Boshra, R. and Kastner, S. (2022). Attention control in the primate brain. *Current Opinion in Neurobiology*, 76:102605.

Bruce, C. J. and Goldberg, M. E. (1985). Primate frontal eye fields. I. Single neurons discharging before saccades. *Journal of Neurophysiology*, 53(3):603–635.

Bruce, C. J., Goldberg, M. E., Bushnell, M. C., and Stanton, G. B. (1985). Primate frontal eye fields. II. Physiological and anatomical correlates of electrically evoked eye movements. *Journal of Neurophysiology*, 54(3):714–734.

Buschman, T. J. and Miller, E. K. (2007). Top-Down Versus Bottom-Up Control of Attention in the Prefrontal and Posterior Parietal Cortices. *Science*, 315(5820):1860–1862.

Cavanagh, S. E., Hunt, L. T., and Kennerley, S. W. (2020). A Diversity of Intrinsic Timescales Underlie Neural Computations. *Frontiers in Neural Circuits*, 14.

Cavanagh, S. E., Wallis, J. D., Kennerley, S. W., and Hunt, L. T. (2016). Autocorrelation structure at rest predicts value correlates of single neurons during reward-guided choice. *eLife*, 5:e18937.

Chaudhuri, R., Bernacchia, A., and Wang, X.-J. (2014). A diversity of localized timescales in network activity. *eLife*, 3:e01239.

Chaudhuri, R., Knoblauch, K., Gariel, M.-A., Kennedy, H., and Wang, X.-J. (2015). A Large-Scale Circuit Mechanism for Hierarchical Dynamical Processing in the Primate Cortex. *Neuron*, 88(2):419–431.

Chen, X., Zirnsak, M., and Moore, T. (2018). Dissonant Representations of Visual Space in Prefrontal Cortex during Eye Movements. *Cell Reports*, 22(8):2039–2052.

Chen, X., Zirnsak, M., Vega, G. M., Govil, E., Lomber, S. G., and Moore, T. (2020). Parietal Cortex Regulates Visual Salience and Salience-Driven Behavior. *Neuron*, 106(1):177–187.e4.

Clark, K. L., Noudoost, B., and Moore, T. (2012). Persistent Spatial Information in the Frontal Eye Field during Object-Based Short-Term Memory. *Journal of Neuroscience*, 32(32):10907–10914.

Constantinidis, C. and Steinmetz, M. A. (2005). Posterior Parietal Cortex Automatically Encodes the Location of Salient Stimuli. *Journal of Neuroscience*, 25(1):233–238.

Demirtaş, M., Burt, J. B., Helmer, M., Ji, J. L., Adkinson, B. D., Glasser, M. F., Van Essen, D. C., Sotiropoulos, S. N., Anticevic, A., and Murray, J. D. (2019). Hierarchical Heterogeneity across Human Cortex Shapes Large-Scale Neural Dynamics. *Neuron*, 101(6):1181–1194.e13.

Dias, E. C. and Segraves, M. A. (1999). Muscimol-Induced Inactivation of Monkey Frontal Eye Field: Effects on Visually and Memory-Guided Saccades. *Journal of Neurophysiology*, 81(5):2191–2214.

Ding, L. and Gold, J. I. (2012). Neural correlates of perceptual decision making before, during, and after decision commitment in monkey frontal eye field. *Cerebral Cortex (New York, N.Y.: 1991)*, 22(5):1052–1067.

Elston, G., Benavides-Piccione, R., Elston, A., Manger, P., and Defelipe, J. (2011). Pyramidal Cells in Prefrontal Cortex of Primates: Marked Differences in Neuronal Structure Among Species. *Frontiers in Neuroanatomy*, 5.

Elston, G. N. (2000). Pyramidal Cells of the Frontal Lobe: All the More Spinous to Think With. *Journal of Neuroscience*, 20(18):RC95–RC95.

Elston, G. N. (2003). Cortex, cognition and the cell: new insights into the pyramidal neuron and prefrontal function. *Cerebral Cortex (New York, N.Y.: 1991)*, 13(11):1124–1138.

Fallon, J., Ward, P. G. D., Parkes, L., Oldham, S., Arnatkevičiūtė, A., Fornito, A., and Fulcher, B. D. (2020). Timescales of spontaneous fMRI fluctuations relate to structural connectivity in the brain. *Network Neuroscience*, 4(3):788–806.

Fisher, N. I. and Marron, J. S. (2001). Mode testing via the excess mass estimate. *Biometrika*, 88(2):499–517.

Gao, R., van den Brink, R. L., Pfeffer, T., and Voytek, B. (2020). Neuronal timescales are functionally dynamic and shaped by cortical microarchitecture. *eLife*, 9:e61277.

Golesorkhi, M., Gomez-Pilar, J., Zilio, F., Berberian, N., Wolff, A., Yagoub, M. C. E., and Northoff, G. (2021). The brain and its time: intrinsic neural timescales are key for input processing. *Communications Biology*, 4(1):1–16.

Hall, P. and York, M. (2001). On the Calibration of Silverman's Test for Multimodality. *Statistica Sinica*, 11(2):515–536.

Hart, E. and Huk, A. C. (2020). Recurrent circuit dynamics underlie persistent activity in the macaque frontoparietal network. *eLife*, 9:e52460.

Hasegawa, R. P., Peterson, B. W., and Goldberg, M. E. (2004). Prefrontal Neurons Coding Suppression of Specific Saccades. *Neuron*, 43(3):415–425.

Hasson, U., Chen, J., and Honey, C. J. (2015). Hierarchical process memory: memory as an integral component of information processing. *Trends in cognitive sciences*, 19(6):304–313.

Heinzle, J., Hepp, K., and Martin, K. A. C. (2007). A Microcircuit Model of the Frontal Eye Fields. *Journal of Neuroscience*, 27(35):9341–9353.

Hüer, J., Saxena, P., and Treue, S. (2024). Pathway-selective optogenetics reveals the functional anatomy of top–down attentional modulation in the macaque visual cortex. *Proceedings of the National Academy of Sciences*, 121(3):e2304511121.

Itti, L. and Koch, C. (2001). Computational modelling of visual attention. *Nature Reviews Neuroscience*, 2(3):194–203.

James, G., Witten, D., Hastie, T., and Tibshirani, R. (2021). Linear Regression. In James, G., Witten, D., Hastie, T., and Tibshirani, R., editors, *An Introduction to Statistical Learning: with Applications in R*, pages 59–128. Springer US, New York, NY.

Lebedev, M. A. (2014). How to read neuron-dropping curves? *Frontiers in Systems Neuroscience*, 8:102.

Litwin-Kumar, A. and Doiron, B. (2012). Slow dynamics and high variability in balanced cortical networks with clustered connections. *Nature Neuroscience*, 15(11):1498–1505.

Lomber, S. G. and Payne, B. R. (2000). Translaminar differentiation of visually guided behaviors revealed by restricted cerebral cooling deactivation. *Cerebral Cortex (New York, N.Y.: 1991)*, 10(11):1066–1077.

Lynch, J. C. and Tian, J.-R. (2006). Cortico-cortical networks and cortico-subcortical loops for the higher control of eye movements. *Progress in Brain Research*, 151:461–501.

Merrikhi, Y., Clark, K., Albarran, E., Parsa, M., Zirnsak, M., Moore, T., and Noudoost, B. (2017). Spatial working memory alters the efficacy of input to visual cortex. *Nature Communications*, 8(1):15041.

Moore, T. and Fallah, M. (2001). Control of eye movements and spatial attention. *Proceedings of the National Academy of Sciences of the United States of America*, 98(3):1273–1276.

Moore, T. and Fallah, M. (2004). Microstimulation of the frontal eye field and its effects on covert spatial attention. *Journal of Neurophysiology*, 91(1):152–162.

Moore, T. and Zirnsak, M. (2017). Neural Mechanisms of Selective Visual Attention. *Annual Review of Psychology*, 68(Volume 68, 2017):47–72.

Murray, J. D., Bernacchia, A., Freedman, D. J., Romo, R., Wallis, J. D., Cai, X., Padoa-Schioppa, C., Pasternak, T., Seo, H., Lee, D., and Wang, X.-J. (2014). A hierarchy of intrinsic timescales across primate cortex. *Nature Neuroscience*, 17(12):1661–1663.

Murray, J. D., Jaramillo, J., and Wang, X.-J. (2017). Working Memory and Decision-Making in a Frontoparietal Circuit Model. *Journal of Neuroscience*, 37(50):12167–12186.

Schall, J. D., Morel, A., King, D. J., and Bullier, J. (1995). Topography of visual cortex connections with frontal eye field in macaque: convergence and segregation of processing streams. *The Journal of Neuroscience: The Official Journal of the Society for Neuroscience*, 15(6):4464–4487.

Stanton, G. B., Bruce, C. J., and Goldberg, M. E. (1995). Topography of projections to posterior cortical areas from the macaque frontal eye fields. *Journal of Comparative Neurology*, 353(2):291–305.

Thompson, K. G., Biscoe, K. L., and Sato, T. R. (2005). Neuronal Basis of Covert Spatial Attention in the Frontal Eye Field. *Journal of Neuroscience*, 25(41):9479–9487.

Wang, X.-J. (2008). Decision Making in Recurrent Neuronal Circuits. *Neuron*, 60(2):215–234.

Wang, X.-J. (2020). Macroscopic gradients of synaptic excitation and inhibition in the neocortex. *Nature Reviews. Neuroscience*, 21(3):169–178.

Wasmuht, D. F., Spaak, E., Buschman, T. J., Miller, E. K., and Stokes, M. G. (2018). Intrinsic neuronal dynamics predict distinct functional roles during working memory. *Nature Communications*, 9(1):3499.

Wolff, A., Berberian, N., Golesorkhi, M., Gomez-Pilar, J., Zilio, F., and Northoff, G. (2022). Intrinsic neural timescales: temporal integration and segregation. *Trends in Cognitive Sciences*, 26(2):159–173.

Wong, K.-F. and Wang, X.-J. (2006). A recurrent network mechanism of time integration in perceptual decisions. *The Journal of Neuroscience: The Official Journal of the Society for Neuroscience*, 26(4):1314–1328.

Xia, R., Chen, X., Engel, T. A., and Moore, T. (2024). Common and distinct neural mechanisms of attention. *Trends in Cognitive Sciences*, 28(6):554–567.

Zeraati, R., Shi, Y.-L., Steinmetz, N. A., Gieselmann, M. A., Thiele, A., Moore, T., Levina, A., and Engel, T. A. (2023). Intrinsic timescales in the visual cortex change with selective attention and reflect spatial connectivity. *Nature Communications*, 14(1):1858.